HiSST: 3rd International Conference on High-Speed Vehicle Science Technology
14 -19 April 2024, Busan, Korea

Radiation Computations and Ionisation Effects for Hypersonic Flow in Thermo-Chemical Nonequilibrium

Dominik James[1], *Christian Mundt*[2]

Abstract

In this work, solutions for atmospheric reentries of two objects are generated: a generic hypersonic glide vehicle and the FIRE II capsule. Two flight points from the FIRE II trajectory are investigated: 1648s and 1636s. Solutions for the flow field are computed with an Euler method. The Euler method is in chemical or thermo-chemical nonequilibrium. An 11-species model allows for ionisation in the inviscid solution. Good agreement has been found for the temperatures and mass fractions along the stagnation line when comparing results to literature. The impact of thermo-chemical nonequilibrium and ions are discussed with regard to radiation.

Keywords: *Ionisation, Hypersonic, Thermo-Chemical Nonequilibrium, HGV, Radiation*

Nomenclature

Latin

$C_{v,trh}$	heavy particle trans.-rot. heat capacity
E	total energy
E_{vib}	vibrational-electronic-electron energy
E_{trh}	heavy particles trans.-rot. energy
n_s	number of species
p	pressure
Q	state vector
S_{vib}	vibr.-electronic-electron source term
t	time
T	translational-rotational temperature
T_{vib}	vibr.-electronic-electron temperature
u_i	Cartesian velocity components (u, v, w)
x_i	Cartesian coordinates (x, y, z)

Greek

δ	Kronecker delta
Δ	step size
$\dot{\omega}_s$	production rate of species s
ρ	mixture density
ρ_s	density of species s

Abbreviations

CFL	Courant-Friedrichs-Lewy number
DOFs	degrees of freedom
KEGS	coupled Euler-boundary layer code
NSMB	Navier-Stokes Multi Block
HGV	hypersonic glide vehicle
RCS	radar cross-section

1. Introduction

High-quality solutions for atmospheric reentries of man-made objects are of great interest for civilian and military applications. The radiation signature of hypersonic objects, such as hypersonic glide vehicles (HGVs), is crucial for their detection. High temperatures in the flow field lead to a strong IR signature. Ions in the wake increase the radar cross-section (RCS). Hence, it is of interest to resolve the temperature in the gas phase and the occurrence of ions in the flow accurately. Thermal nonequilibrium leads to higher temperatures behind the shock than thermal equilibrium. General approaches like Reynolds-averaged Navier-Stokes simulations or Large Eddy Simulations have undesirably long computation times for design work. The specialised Euler-boundary layer method used in this work, KEGS, can deliver comparable accuracy at a much shorter computation time.

[1] *Universität der Bundeswehr München, Werner-Heisenberg-Weg 39, 85579 Neubiberg, dominik.james@unibw.de*
[2] *Universität der Bundeswehr München, Werner-Heisenberg-Weg 39, 85579 Neubiberg, christian.mundt@unibw.de*

In 2020, KEGS has generated 2D chemical nonequilibrium results for a generic triple cone and the 1648s flight point of the Fire II experiment using a 5-species model [1]. 3D equilibrium solutions for a generic hypersonic glide vehicle at Mach 10 and 30km altitude were generated in 2022 [2]. First results for 2D thermo-chemical nonequilibrium (5-species) for the FIRE II 1648s flight point were presented in 2023 [3]. A finite-difference method similar to the one used in this work was developed by Ghezali et al. in 2018 [4]. They investigated different thermo-chemical models in 1D and give results for the stagnation line of the 1634s and 1643s flight points of FIRE II. Niu et al. [5] investigated how different angles of attack influence the infrared radiation characteristics of a hypersonic glide vehicle (HTV-2) in 2019. In 2022 Yu et al. [6] developed and applied a band detection method to a generic HGV. They found that using an optimized spectral band depending on the background and trajectory point of the HGV increases detection efficiency.

For this work, an 11-species model is added to KEGS to investigate the effect of ionisation. Additionally, electron effects are considered in the source term for thermal nonequilibrium. Two flight points of FIRE II investigated: 1648s (8.2km/s inflow velocity at 41km altitude), and 1636s (11.31km/s inflow velocity at 71km altitude). The conditions at 1648s are in chemical nonequilibrium with small thermal nonequilibrium effects. The conditions at 1636s are in thermo-chemical nonequilibrium.

2. Theoretical Considerations

In regions of chemical nonequilibrium the relaxation time for chemical reactions is comparable with the shock stand-off distance. The composition cannot be assumed to be in equilibrium behind the shock. That means for each species a separate conservation of mass equation must be solved. Treating the chemical source term explicitly (first-order Euler forward method) is only stable at 1636s (higher altitudes) and if no electrons are considered. Treating the chemical source term point-implicitly (first-order Euler backward method) is stable for both flight points and the 11-species model.

The 17-reaction, 5-species model of Park 1985 contains the species N, N_2, O, O_2, and NO [4]. Ionisation is possible in the 11-species model which additionally contains their ions and electrons. The 47 reactions allow for impact dissociation, exchange reactions, associative ionisation, and electron impact ionisation.

Thermo-chemical nonequilibrium occurs at even more extreme conditions where the relaxation time for internal degrees of freedom (DOFs) is not negligible anymore. Now, not only the chemical composition is not in equilibrium but also the internal DOFs. The DOFs are separated into two groups for this work and each group is assigned its own temperature: the heavy particle translational-rotational temperature T and the vibrational-electronic-electron temperature T_{vib}.

Translational DOFs and rotational DOFs of heavy particles only need a few collisions to reach equilibrium and are therefore assumed to be in equilibrium in the entire flow field. Vibrational, electronic and electron translational DOFs need many more collisions, i.e., are slower to reach equilibrium. For them, an additional governing equation for the vibrational-electronic-electron energy, E_{vib}, is solved. T_{vib} and T are different in regions of thermal nonequilibrium (e.g., behind the shock), and equal in regions of thermal equilibrium. Treating electron translational DOFs separate from heavy particles' translational DOFs is justified due to the rapid relaxation between electron translational DOFs and vibrational modes of N and O [8].

3. Numerical Method

This chapter gives an overview of the shock-fitting finite difference method and a detailed description of the newly added 11-species model and the thermal nonequilibrium source term.

3.1. Solution Procedure

First, the Euler solution is generated. Next, the boundary layer solution is iteratively calculated until its profile at the outer edge fits to the inviscid solution. Then, a new Euler solution is computed accounting for the boundary layer solution via an equivalent source distribution. Another calculation of the boundary layer for the new Euler field concludes the flow field computations. In this work the focus lays on the Euler method.

The CFL number has been set to 1 for 1648s. Values as high as 1.6 lead to converging solutions. For 1636s CFL values around 0.1-0.3 are successful for thermo-chemical nonequilibrium.

3.2. Governing Equations

The governing equations for inviscid thermo-chemical nonequilibrium flow are given in vector form in Eq. 1; where Q is the state vector, f_i are the inviscid fluxes, and S is the source term.

These equations are transformed onto a curvilinear system and the transformed fluxes are similarity transformed to increase computation speed. Then, they are eigendecomposed and the eigenvalues are split according to their signs (flux vector splitting). This is a crucial step to achieve a stable algorithm. The spatial discretization is a third-order upwind-biased finite difference scheme. The upwind direction is based on the sign of the eigenvalues. In time, the equations are integrated using a low-storage second-order 3-step Runge-Kutta scheme.

$$\frac{\partial}{\partial t}\underbrace{\begin{bmatrix}\rho\\ \rho u\\ \rho v\\ \rho w\\ \rho_1\\ \vdots\\ \rho_{n_s}\\ \rho E\\ \rho E_{vib}\end{bmatrix}}_{Q}+\sum_{x_i=(x,y,z)}\frac{\partial}{\partial x_i}\underbrace{\begin{bmatrix}\rho u\\ \rho u u_i+\delta_{1i}p\\ \rho v u_i+\delta_{2i}p\\ \rho w u_i+\delta_{3i}p\\ \rho_1 u_i\\ \vdots\\ \rho_{n_s}u_i\\ (\rho E+p)u_i\\ \rho u_i E_{vib}\end{bmatrix}}_{f_i}=\underbrace{\begin{bmatrix}0\\ 0\\ 0\\ 0\\ \dot{\omega}_1\\ \vdots\\ \dot{\omega}_{n_s}\\ 0\\ S_{vib}\end{bmatrix}}_{S} \tag{1}$$

3.3. Equations of State

The flow is assumed to be a mixture of ideal gases for the thermal equation of state. The pressure is computed using Dalton's law of partial pressures.

For the 5-species caloric equation of state, a polynomial fit for the mass-specific species enthalpies from Warnatz can be used [8]. As an alternative, and for the 11 species model, the energies for the different internal degrees of freedom are computed separately and then summed up. Vibrational and electronic energies are computed assuming a harmonic oscillator model [10]. The sum of heavy particle translational and rotational, vibrational, electronic, translational electron, and chemical formation energy is equal to the total internal energy. In thermal equilibrium T can then be found by using Newton's method. The enthalpy is evaluated for different T until it matches the enthalpy computed from the state vector.

In thermal nonequilibrium, a second caloric equation of state is needed to compute T_{vib}. This equation is E_{vib}, computed as the sum of vibrational, electronic, and electron energies. E_{vib} from the state vector is subtracted from the second caloric equation of state (dependent on T_{vib}). Newton's method can then be used to solve for T_{vib}. Computing T in thermal nonequilibrium does not require iteration because translational-rotational DOFs are assumed fully activated at all temperatures of interest which means their heat capacities are constant. Hence, subtracting E_{vib} from E in the state vector gives the translational-rotational energy for heavy particles and T can be computed with the reference temperature of 298.15K directly from $E_{trh} = C_{v,trh}(T - T_{\mathrm{ref}})$.

3.4. Nonequilibrium Chemistry

The chemistry model is Park's 1985 model [4]. The inflow mole fractions are set to 79.27% N_2 and 20.73% O_2. Across the shock the composition will change significantly through chemical reactions.

To compute the change in species densities since the last time step, explicit treatment can be used. The first-order forward Euler method then gives:

$$\rho_i^{(n+1)} = \rho_i^{(n)} + \underbrace{\dot{\omega}_i^{(n)}(T,\rho_s)\cdot\Delta t}_{\Delta\rho_{i,\mathrm{explicit}}} \tag{2}$$

Since this created numerical problems, a point-implicit method was constructed from the first-order backward Euler method:

$$\rho_i^{(n+1)} = \rho_i^{(n)} + \underbrace{\dot{\omega}_i^{(n+1)}(T, \rho_s) \cdot \Delta t}_{\Delta\rho_{i,\text{implicit}}} \tag{3}$$

$$\dot{\omega}_i^{(n+1)} = \dot{\omega}_i^{(n)} + \sum_j \left[\frac{d\dot{\omega}_i^{(n)}}{d\rho_j}\right] \cdot \Delta\rho_i \tag{4}$$

Combining these equations, and collecting the $\Delta\rho_i$ terms, gives a system of linear equations which must be solved to compute the change in species densities:

$$\sum_j \left[\frac{\delta_{ij}}{\Delta t} - \frac{d\dot{\omega}_i^{(n)}}{d\rho_j}\right] * \Delta\rho_i = \dot{\omega}_i^{(n)} \tag{5}$$

The system of equations can be simplified for the inviscid calculation. Since the number of elementary particles must be the same before and after the reactions, changes of N_2, O_2 and electrons can be deduced from the others. This reduces the system to 3x3 for 5-species and 8x8 for 11-species. 3x3 matrices can be inverted analytically; the 8x8 system can be solved via partial pivoting and then LU decomposition. Solving the full 11x11 system is difficult because the system is very ill-conditioned. The reduction to 8x8 reduces the stiffness which helps to get an accurate numerical solution.

For the 11-species model the stiffness is stronger than for 5 species due to the additional fast electron impact reactions. The stiffness is also worse at lower temperatures. Hence, ions are assumed to form only above 3000K. This results in a generally stable algorithm.

3.5. Thermal Nonequilibrium Source Terms

For 5 species, there are two components for the source term of E_{vib}: (1) Production of E_{vib} through chemical reactions involving molecules; and (2) relaxation between translational-rotational DOFs of heavy particles and vibrational-electronic-electron DOFs.

(1): If a molecule dissociates, its vibrational-electronic energy is converted to translational energy of the reaction products. This decreases E_{vib}. The reverse process, recombination, increases E_{vib}. The preferential model assumes that molecules in a higher vibrational state are more likely to dissociate. Hence, a dissociation converts more vibrational-electronic energy than the average level. This can lead to vibrational temperatures well below the inflow temperature directly behind the shock because of the strong dissociations. The non-preferential model assumes that the average vibrational-electronic energy level is converted which does not lead to a drop of T_{vib}.

(2): The temperature difference between T and T_{vib} drives the relaxation process between translational-rotational and vibrational-electronic-electron modes. It is computed with the semi-empirical correlation for the vibrational-translational relaxation from Millikan and White [11] with the high-temperature correction from Park [9]. Scalabrin [10] assumes fast energy transfer between vibrational, electronic and electron modes and thus expands the relaxation to all internal energy modes. This assumption is made in this work as well.

For 11 species, two additional source term components are considered: (3) Production of E_{vib} through electron impact ionisation; and (4) relaxation between electrons and heavy particles through elastic collisions.

(3): If an electron impacts a heavy particle and frees another electron, then the energy for the ionisation comes at least partially from the impacting electron. This energy is then removed from E_{vib}. Setting the energy to the first ionisation energy is an overestimation that sometimes leads to negative values for T_{vib}. Scalabrin [10] therefore sets it to around one third of the first ionisation energy which is also done in this work. There are only two such reactions in the 11 species model.

(4): The energy transfer between electrons and heavy particles is modelled as in [10], with a constant collision cross-section for electron-neutral collisions, and a collision cross-section dependent on T_{vib} for electron-ion collisions.

3.6. Thermo-Chemical Nonequilibrium Shock Layer

To reduce the gradients appearing in the Euler flow field, a 1D shock tube integration is carried out for the region directly behind the shock to get integrated values for the mass fractions and E_{vib} that serve as boundary condition for the Euler algorithm.

The shock is assumed to consist of a sharp wave front (left interface), a shock layer in thermo-chemical nonequilibrium in the middle, and a right-side interface to the Euler algorithm, see Fig. 1. The left interface is assumed so thin that no reactions happen going across. ρ, p and T increase, but y_s stays the same.

For thermal nonequilibrium it is assumed that only translational-rotational DOFs of heavy particles accommodate to the new conditions, i.e. T_{vib} does not change going across. This means the kinetic energy by which the flow slowed down across the shock is stored only by heavy particle translational-rotational DOFs. T increases more in thermal nonequilibrium because the vibrational-electronic-electron energy does not change across the left interface.

Fig. 1 Thermo-chemical nonequilibrium shock layer with interfaces

Next, in the shock layer the source terms for chemical and thermal nonequilibrium are integrated in many small steps with a 1st-order explicit Euler method to get integrated values for the mass fractions y_s and E_{vib}. A parameter study was conducted to find a threshold for the maximal change per step such that the final values are accurate to 0.1%. The threshold is realized via step-size control.

For each step, the temperature and mixture density at the current position are computed using the Rankine-Hugoniot conditions. Then, based on the mass flux, mixture density, and spatial step size the time step Δt (how long the flow spends in this step) is computed. With the time step and temperature, the change in mass fractions due to chemical reactions is computed. For thermal nonequilibrium E_{vib} is integrated according to the source term components described above.

The thickness of this shock layer is set to 6 mean free paths for 1648s (0.125mm), and 0.5 mean free paths for 1636s (0.362mm); and is assumed constant for the entire shock contour. As it is only 1D, it should be small compared to the shock stand-off distance and not reach the equilibrium region. A parameter study with different thicknesses showed differences below 1% for different thicknesses. The thicker the layer, the fewer nodes are needed in the Euler algorithm to resolve the strong gradients behind the shock. This leads to faster computation times.

The right-side interface then serves y_s and E_{vib} as boundary condition for the Euler algorithm.

4. Results

The 11-species model and the thermal nonequilibrium are new features in the Euler code. Hence, they are validated against reference data for the FIRE II 1636s flight point which features thermo-chemical nonequilibrium with ions.

Then results for a generic hypersonic glide vehicle at the same conditions are presented.

4.1. Comparison of 1636s FIRE II Case to Literature

The temperature distribution on the stagnation line of the newly implemented 11-species thermo-chemical nonequilibrium Euler method is compared to reference data of Göbel et al. [12]. There are two differences between the physical models: Firstly, [12] used a 13-species model which also includes Argon and its ion. Since Argon is non-reactive and makes up less than 1% of the inflow by mole fraction, the difference in results should be small. Secondly, Göbel et al. associated each molecule with its own vibrational temperature, while in the Euler method one vibrational temperature is used for all molecules.

Separate vibrational temperatures require knowledge of more physical constants of which some are not well-known [9]. Additionally, as shown in the data of Göbel, separate vibrational temperatures bring numerical issues, especially when the mole fraction of the associated molecule is low. Thus, in [12], the vibrational temperature of O_2 is used as T_{vib}. Since computational effort also increases with the inclusion of a separate governing equation for an E_{vib} for each molecule, the Euler method uses a single T_{vib} for all molecules.

The boundary condition at the shock is different due to the code architectures: The Euler method is shock-fitting while NSMB, the code used by Göbel et al., is shock-capturing. The computational domain for shock-fitting methods starts right at the shock. Shock-capturing methods on the other hand also resolve the inflow before the shock for a small distance. For shock-capturing methods T increases smoothly from its inflow value, and chemical reactions start to happen immediately. These reactions reduce the maximum T reached compared to the shock-fitting method employed here, where the entire kinetic energy freed through the shock is used to increase T. With this in mind, the temperatures on the stagnation line in Fig. 2 are in good agreement.

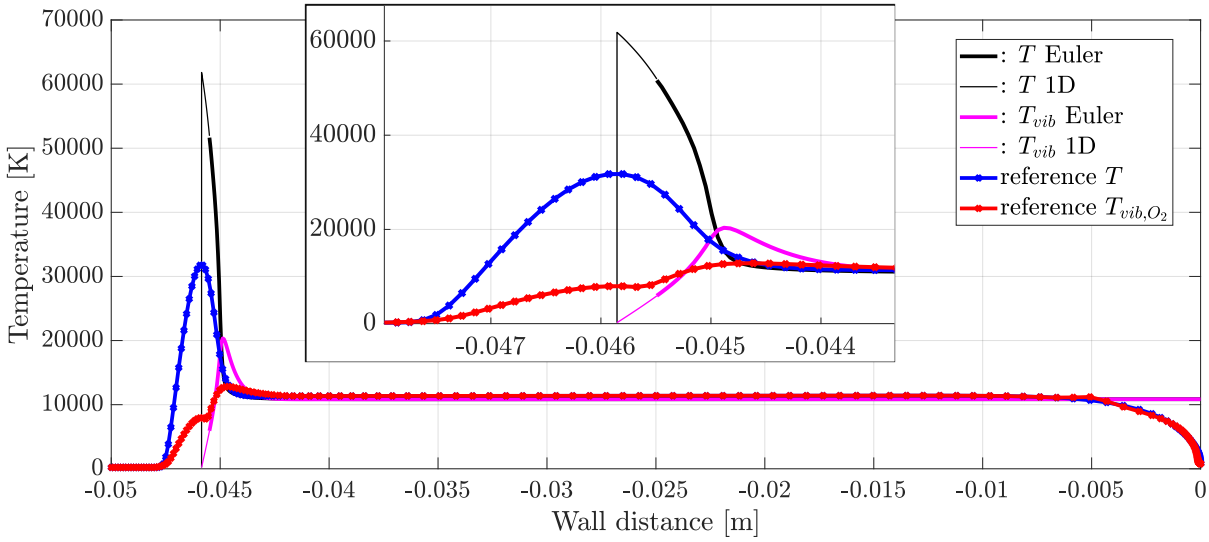

Fig. 2 Comparison of 11-species thermo-chemical nonequilibrium shock-fitting Euler result with 13-species thermo-chemical nonequilibrium shock-capturing NSMB result [12] on the stagnation line

When T and T_{vib} are equal, the flow is in thermal equilibrium. For the Euler method the first 6.5% of the shock stand-off distance, or about 3.0mm, are in thermal nonequilibrium when defining equilibrium as $|T_{vib}/T - 1| < 1\%$. When measuring from the peak of T for the NSMB result, it is 8.3% or 3.8mm.

The T computed in this work is close to the T of [12] in the equilibrium region. The small difference is attributed to the different equilibrium constants in the chemical-kinetic model: The Euler method uses Park 1985, while [12] used Park 1989. The difference between T_{vib} and T at the end of the equilibrium region (at the wall) is in the order of 1E-6 for the Euler method.

In the shock-fitting case, the higher values of T at the wave front of the shock lead to a larger difference between T and T_{vib} which give rise to a greater production of E_{vib} through relaxation, compared to the shock-capturing result. Hence a higher maximum T_{vib} is reached compared to T_{vib,O_2}. The local minimum in the middle of the shock of [12] is not expected from a physical perspective and is likely a numerical issue. T_{vib} of the Euler method does not exhibit this problem. It increases monotonically until it reaches a maximum shortly after crossing T because the finite relaxation time of the internal DOFs gives the development of E_{vib} inertia.

Therefore, T_{vib} overshoots T slightly, and then decreases again towards T. $T - T_{vib}$ behaves like a strongly damped oscillation with increasing period. Within the shock stand-off distance two overshoots and two undershoots are happening, with only the first overshoot being of significant magnitude.

At the shoulder of the vehicle the region of thermal nonequilibrium behind the shock is larger than at the stagnation point, see Fig. 3 a) and b). Additionally, the region near the bend is also in thermal nonequilibrium. T responds directly to the expansion of the flow and drops significantly at the bend, see Fig. 3 c). The resulting temperature difference $T - T_{vib}$ then drives the relaxation of T_{vib}, see Fig. 3 d). The finite relaxation time corresponds to the size of the thermal nonequilibrium region.

Fig. 4 a) shows the mole fraction of electrons which corresponds to the degree of ionisation. The highest fraction of ions is reached behind the shock on the stagnation line with about 15%. The degree of ionisation decreases away from the stagnation line. 15% is not negligible, and ionisation should be considered for this case.

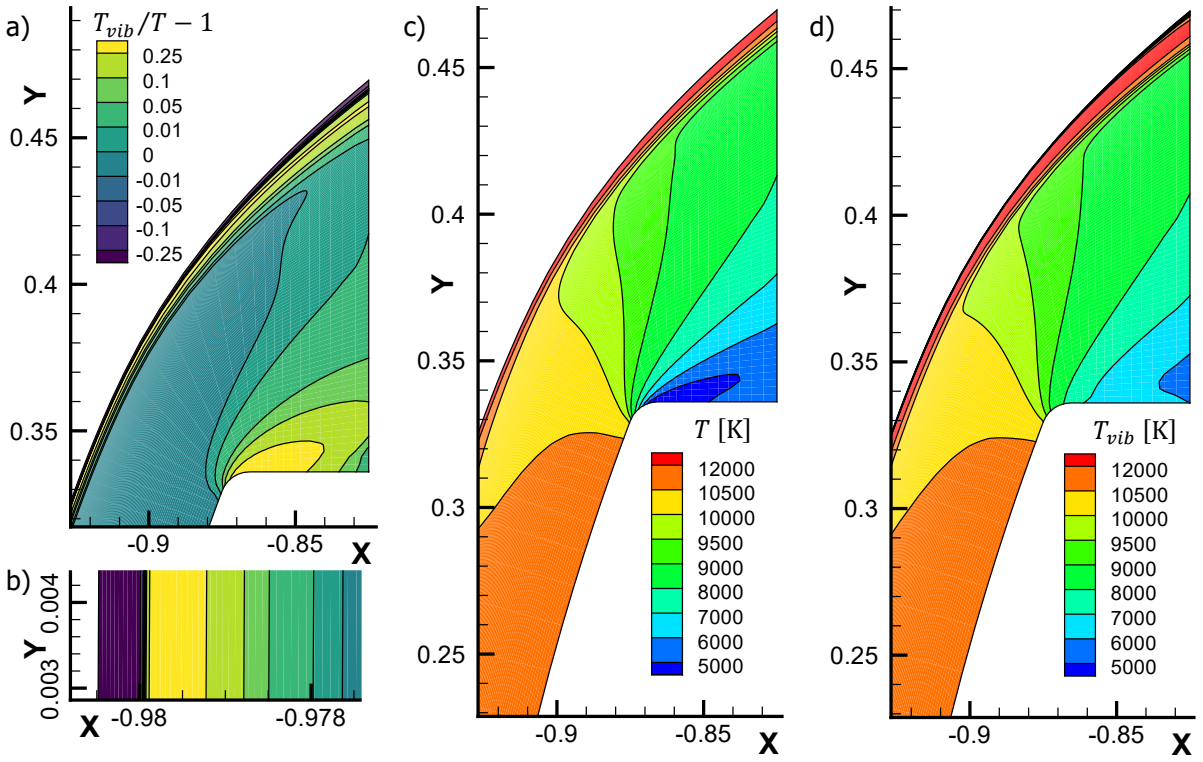

Fig. 3 Temperature ratio $T_{vib}/T-1$ in region of a) shoulder and b) stagnation; c) T and d) T_{vib} in the expansion region around the shoulder

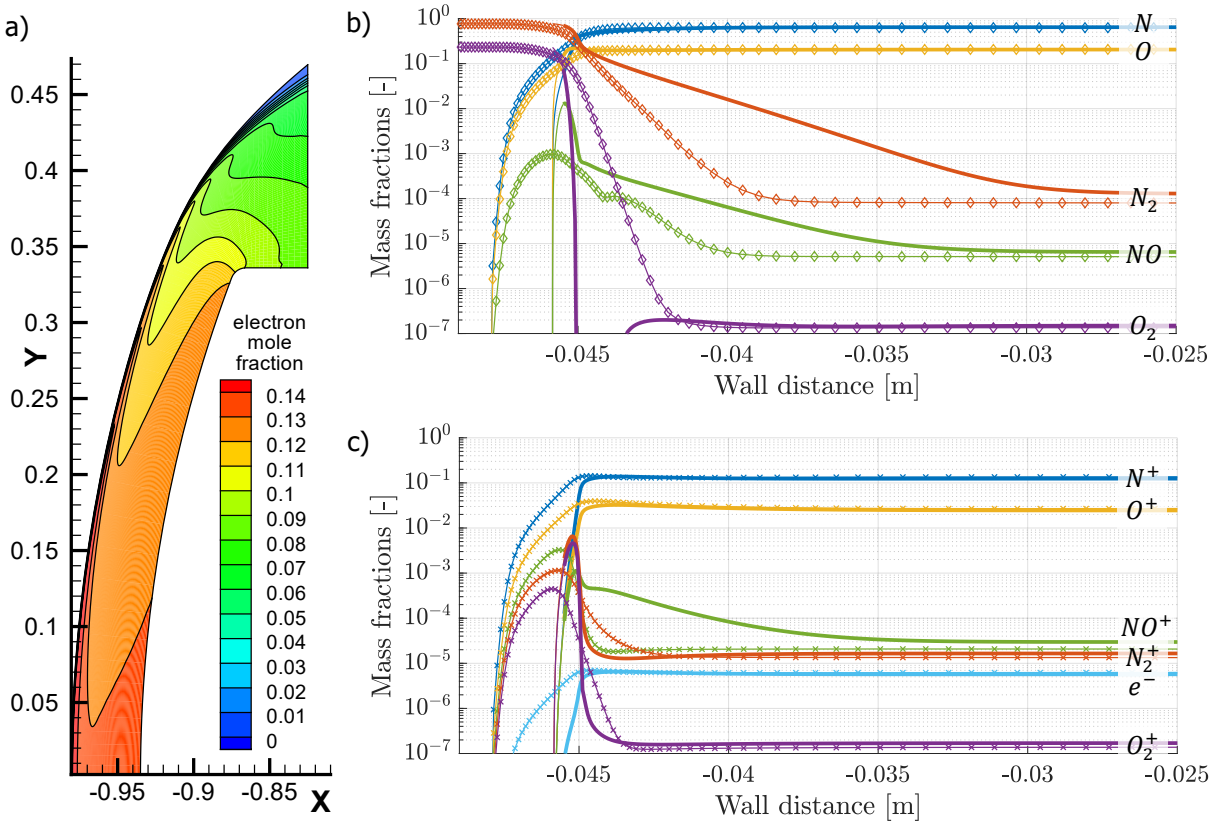

Fig. 4 a) Electron mole fraction (degree of ionisation); mass fractions on stagnation line of b) of neutral particles and c) charged particles

The mass fractions on the stagnation line are compared to reference data of [12] in Fig. 4 b) for neutral and c) for charged particles. The dominant ions are N^+ and O^+. The equilibrium values are close for all species. Differences are attributed to the different chemical kinetic models. If ions form, the equilibrium temperature will be lower because their formation energy is very high. Simulations for 5 species resulted in an equilibrium temperature of about 19,500K which is almost twice as high as with 11 species. This underlines the necessity of including ions for the present case.

4.2. Generic Hypersonic Glide Vehicle

Aerothermodynamic loads for a 3D generic hypersonic glide vehicle in thermo-chemical equilibrium have been computed in [2]. The nose region experiences the highest temperatures and strongest gradients and is therefore the most interesting with regards to radiation. For Mach 25 at 30km altitude a 3D equilibrium solution for the temperature field is given in Fig. 5 a). In Fig. 5 b) a 2D rotationally symmetric thermo-chemical nonequilibrium solution with 5 species at the 1648s flight point (Mach 25.6 at 41km altitude) is given for the lower side of the HGV nose in the symmetry plane (see arrow). The temperature behind the shock is significantly higher for the thermo-chemical nonequilibrium solution. The emitted radiation will therefore be stronger.

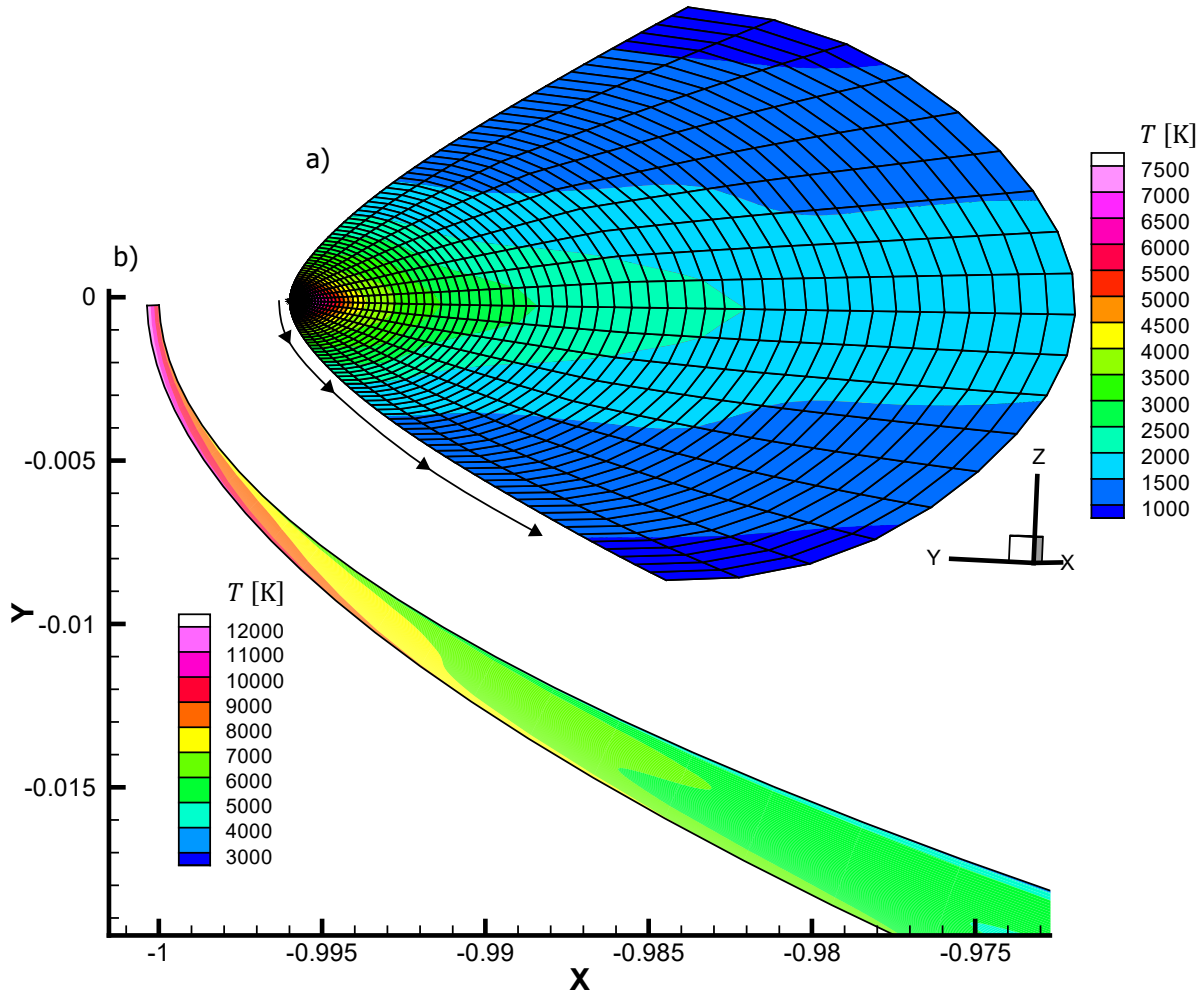

Fig. 5 3D equilibrium solution for T of a generic HGV at 30km altitude at Mach 25

The shock stand-off distance scales with the nose radius. Since the nose radius of the HGV is much smaller than the nose radius of the FIRE II capsule, the HGV's shock stand-off distance is much smaller as well. The 5-species model is also slower to decrease the high temperature behind the shock through chemical reactions because it cannot form ions. Therefore, it is slower to reach equilibrium than the 11-species model. Near the stagnation point neither the 5-species nor the 11-species model reach equilibrium conditions until the wall.

4.3. Radiation

Radiant emittance is proportional to the fourth power of T, as described by the Stefan-Boltzmann law. It is therefore important to resolve the temperature in the gas phase accurately. The total emission has been computed in [13] for the FIRE II 1636s result of [12]. The results in Fig. 6 show the strong dependence of the total emission on the temperature T. The emission is strongest where the temperature is highest. Therefore, it is important to resolve the thermal nonequilibrium at the shock in the numerical simulation.

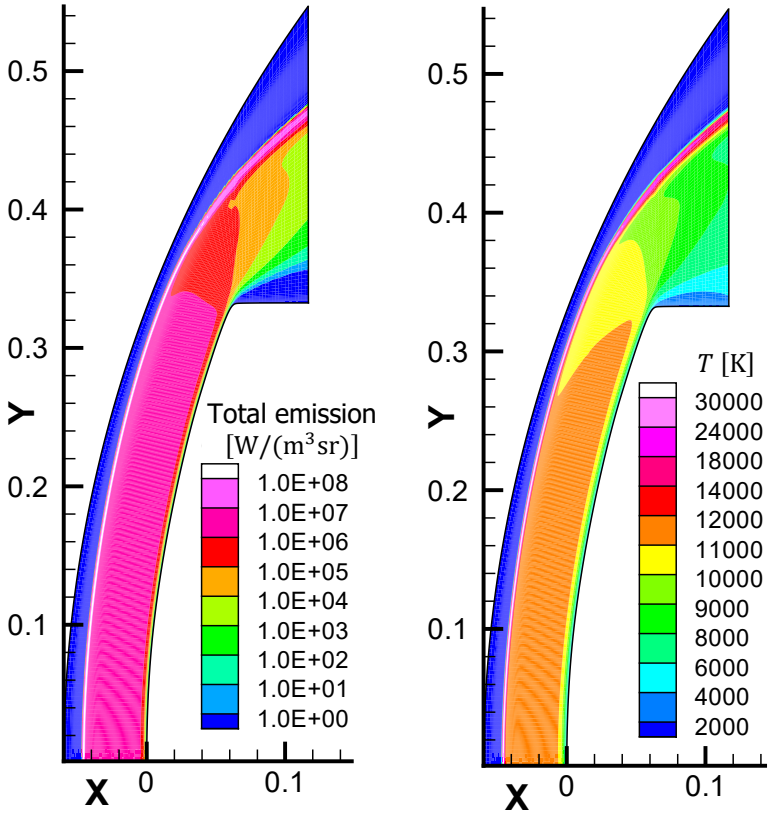

Fig. 6 Total emission [13] and temperature [12] of FIRE II 1636s case

If the wake of an object contains even a low percentage of ions, then its radar cross section (RCS) increases. Hence, numerical simulations of ionized flows are of considerable interest as they can give information about the composition of the wake. For the two cases investigated in this work, both exhibit ionisation of the flow. The FIRE II 1636s case has a higher maximum degree of ionisation (15%) due to its higher velocity; the maximum ionisation for the HGV at 1648s for the 11-species thermo-chemical nonequilibrium model is 13% but drops quickly along the body of the HGV.

5. Conclusion

An 11-species model in thermo-chemical nonequilibrium was implemented into a shock-fitting Euler method. Converged results were obtained for the FIRE II capsule at 1636s and a generic HGV at the conditions of the 1648s flight point. Results for the FIRE II 1636s case were compared to literature and show good agreement for temperatures and mass fractions on the stagnation line.

The flow fields for the FIRE II capsule and the generic HGV feature ionisation. The fraction of ions is largest near the stagnation line and drops towards the rear. Ions in the wake of the body increase the radar cross-section which is important for detecting high-speed objects. Thermal nonequilibrium increases the maximum temperature reached in the gas phase at the shock compared to a thermal equilibrium assumption. This is important for the radiation signature as the radiant emittance is strongly dependent on temperature.

References

1. J. Bonin: Untersuchung der optischen Abstrahlung von ballistischen Flugkörpern unter Berücksichtigung der Kopplung von Strömung und Strahlung. (Investigation of optical radiation of ballistic spacecrafts considering the coupling of flow and radiation). Dissertation, Universität der Bundeswehr München, (2020).
2. D. Hauger, J. Bonin, Ch. Mundt: Studie über aerothermodynamische Lasten eines hypersonischen Gleiters. (Study of aerothermodynamic loads on a hypersonic glider). DWT Conference, Bonn, Germany, (2022).
3. D. James, Ch. Mundt: Aerodynamic Loads of Thermo-Chemical Nonequilibrium Hypersonic Flow Around a Generic HGV. 15th 3AF Int. Conf., Integrated Air and Missile Defense, Porto, Portugal, (2023).
4. Y. Ghezali, R. Haoui, A. Chpoun: Study of physico-chemical phenomena in a non-equilibrium hypersonic air flow behind a strong shock wave. Thermophys. Aeromech. 26, 693–710, (2019). https://doi.org/10.1134/S086986431905007X
5. Q. Niu, Z. Yuan, B. Chen, S. Dong: Infrared radiation characteristics of a hypersonic vehicle under time-varying angles of attack. Chinese Journal of Aeronautics, Volume 32, Issue 4, Pages 861-874, (2019). https://doi.org/10.1016/j.cja.2019.01.003
6. S. Yu, X. Ni, X. Li, T. Hu, F. Chen: Real-time dynamic optimized band detection method for hypersonic glide vehicle. Infrared Physics & Technology, Volume 121, (2022). https://doi.org/10.1016/j.infrared.2022.104020
7. C. Park: On Convergence of Computation of Chemically Reacting Flows. AIAA-85-0247, AIAA 23rd Aerospace Sciences Meeting, Reno, Nevada, (1985). https://doi.org/10.2514/6.1985-247
8. M. Pfitzner: A Shock-fitting Algorithm for the Simulation of Inviscid Flows in Chemical Non-Equilibrium. In: Morton, K.W. (eds) 12th International Conference on Numerical Methods in Fluid Dynamics. Lecture Notes in Physics, vol 371. Springer, Berlin, Heidelberg, (1990). https://doi.org/10.1007/3-540-53619-1_230
9. P. A. Gnoffo, R. N. Gupta, J. L. Shinn: Conservation Equations and Physical Models for Hypersonic Air Flows in Thermal and Chemical Nonequilibrium. NASA Technical Paper 2867, (1989).
10. L. Scalabrin: Numerical Simulation of Weakly Ionized Hypersonic Flow Over Reentry Capsules. Dissertation, The University of Michigan, (2007).
11. R. C. Millikan, D. R. White: Systematics of Vibrational Relaxation. J. Chem. Phys. 15; Volume 39 Issue 12: 3209–3213, (1963). https://doi.org/10.1063/1.1734182
12. F. Göbel, J. Vos, Ch. Mundt: CFD Simulation of the FIRE II Flight Experiment. AIAA-2012-3350, 42nd AIAA Fluid Dynamics Conference and Exhibit, (2012). https://doi.org/10.2514/6.2012-3350
13. Ch. Mundt, D. James: Photon Monte Carlo transport computation for atmospheric (re-)entry. 9th ESA International Workshop on Radiation of High Temperature Gases in Atmospheric Entry, St. Maria, Azores, (2022).